Earth, Planets and Space

FULL PAPER Open Access

Weakening behavior of the shallow megasplay fault in the Nankai subduction zone

Alexander Roesner, Matt J. Ikari*, Andre Hüpers and Achim J. Kopf

Abstract

The Nankai Trough megasplay fault hosts diverse modes of fault slip, ranging from slow slip events to megathrust earthquakes, and is responsible for related phenomena such as tsunamis and submarine landslides. All types of slip events require some kind of frictional weakening process in order to nucleate and propagate. We tested fluid-saturated, powdered megasplay fault samples in a direct shear apparatus under effective normal stresses of 2–18 MPa to investigate their friction velocity- and slip-dependence. The experiments show that for short distances (1 mm) after a velocity step, there is an evolution from velocity weakening at low effective normal stress to velocity strengthening at high effective normal stresses. Over a longer distance (5 mm), large velocity weakening is observed over all tested effective normal stresses. In all experiments, slip weakening behavior occurred with relatively large weakening rates at low effective normal stresses and smaller weakening rates at higher effective normal stresses. Critical stiffnesses for slip instability were calculated for both the velocity and slip dependence of friction to determine their relative importance. At shallow depths, velocity weakening would be the main cause of frictional instability for both small and large slip perturbations, whereas at greater depth instability requires either slip weakening over small slip distances, or velocity weakening induced by larger slip. Regardless of the underlying mechanism, the observed slip instability at lower effective stresses increases the likelihood for fault slip events to travel to the seafloor which may cause submarine landslides and tsunamis.

Keywords: Nankai Trough, Slip weakening, Velocity weakening, Megasplay fault, Friction, Slip dependence, Subduction zone, Japan

*Correspondence: mikari@marum.de

MARUM - Center for Marine Environmental Sciences, University Bremen, Bremen, Germany

Graphical Abstract

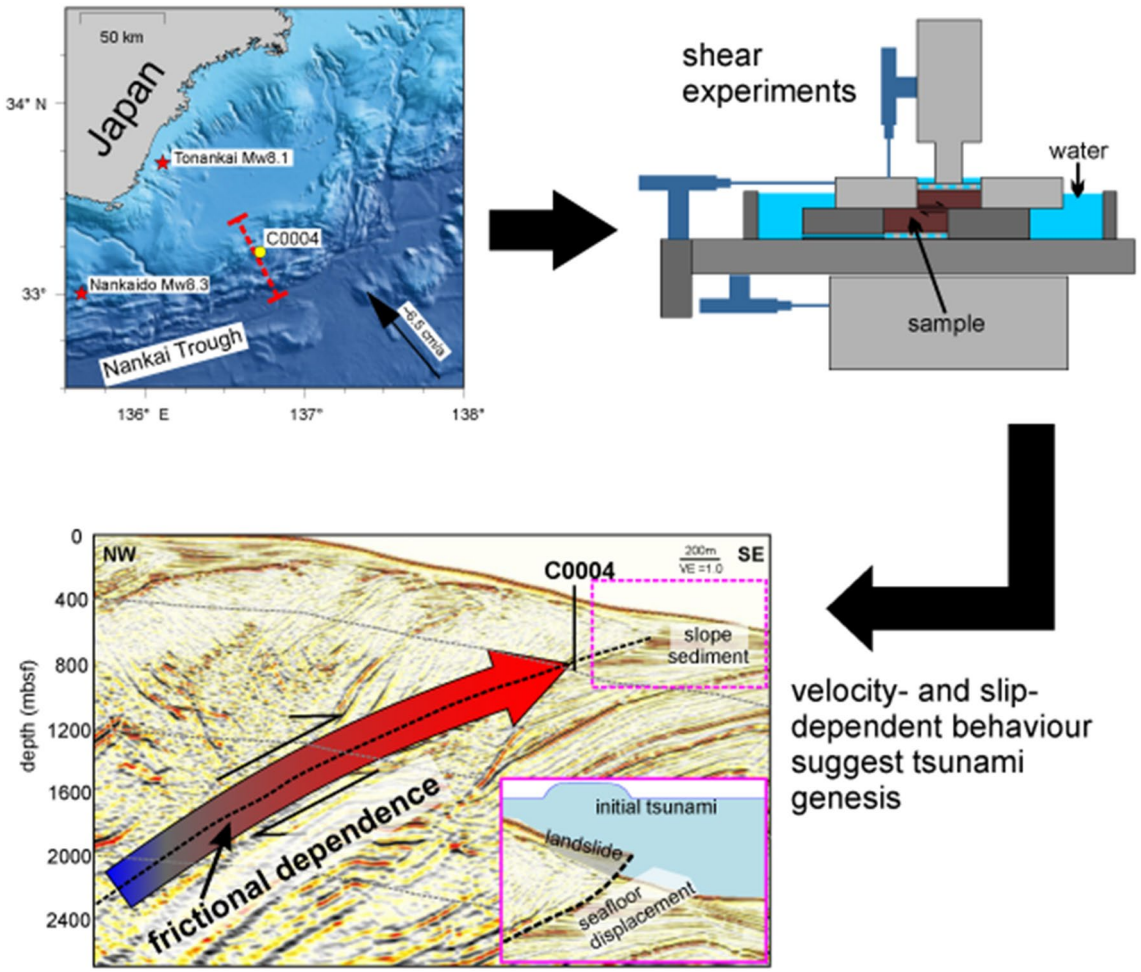

Introduction

The Nankai Trough subduction zone offshore SW Japan has a long history of documented large-magnitude megathrust earthquakes with recurrence intervals of 90–150 years (Ando 1975a). In the last century, two megathrust earthquakes with $M_w > 8$ occurred in the Nankai Trough (Ando 1982; Tanioka and Satake 2001) (Fig. 1A). One of these, the 1944 Tonankai earthquake, triggered a tsunami with an average wave height of 6–8 m along the Kumano coast (Ichinose et al. 2003). Over the last 400 years, five megathrust earthquakes generated devastating tsunamis of various intensity that hit the coastline along the Nankai Trough (Ando 1975b). Frictional heating documented by vitrinite reflectance in ocean drilling samples of a major out-of-sequence thrust fault and the toe of the Nankai accretionary prism suggests that coseismic slip extended close to the seafloor along these faults (Sakaguchi et al. 2011). In recent years, a comprehensive spectrum of fault slip modes including very low frequency earthquakes (VLFEs) (Ito and Obara 2006; Obara and Ito 2005; Sugioka et al. 2012), slow slip events (SSEs) (Araki et al. 2017; Hirose et al. 2010; Nakano et al. 2018), and tectonic tremor (Annoura et al. 2017; Ide 2012) have been documented in the Nankai Trough subduction zone from the outer accretionary prism up to the trench (Fig. 1). The type of shallow fault slip events are important for evaluating tsunami earthquake and tsunami hazards in general (Polet and Kanamori 2000), but the role played by frictional properties in shallow slip remains subject to debate (Bilek and Lay 2002; Faulkner et al. 2011; Marone and Scholz 1988; Seno 2002).

In general, fault slip behavior is thought to be controlled by the frictional properties of the fault gouge, which is often quantified by measurements of rate- and state-dependent friction (RSF) that describes the frictional stability of rocks and sediments (Marone 1998).

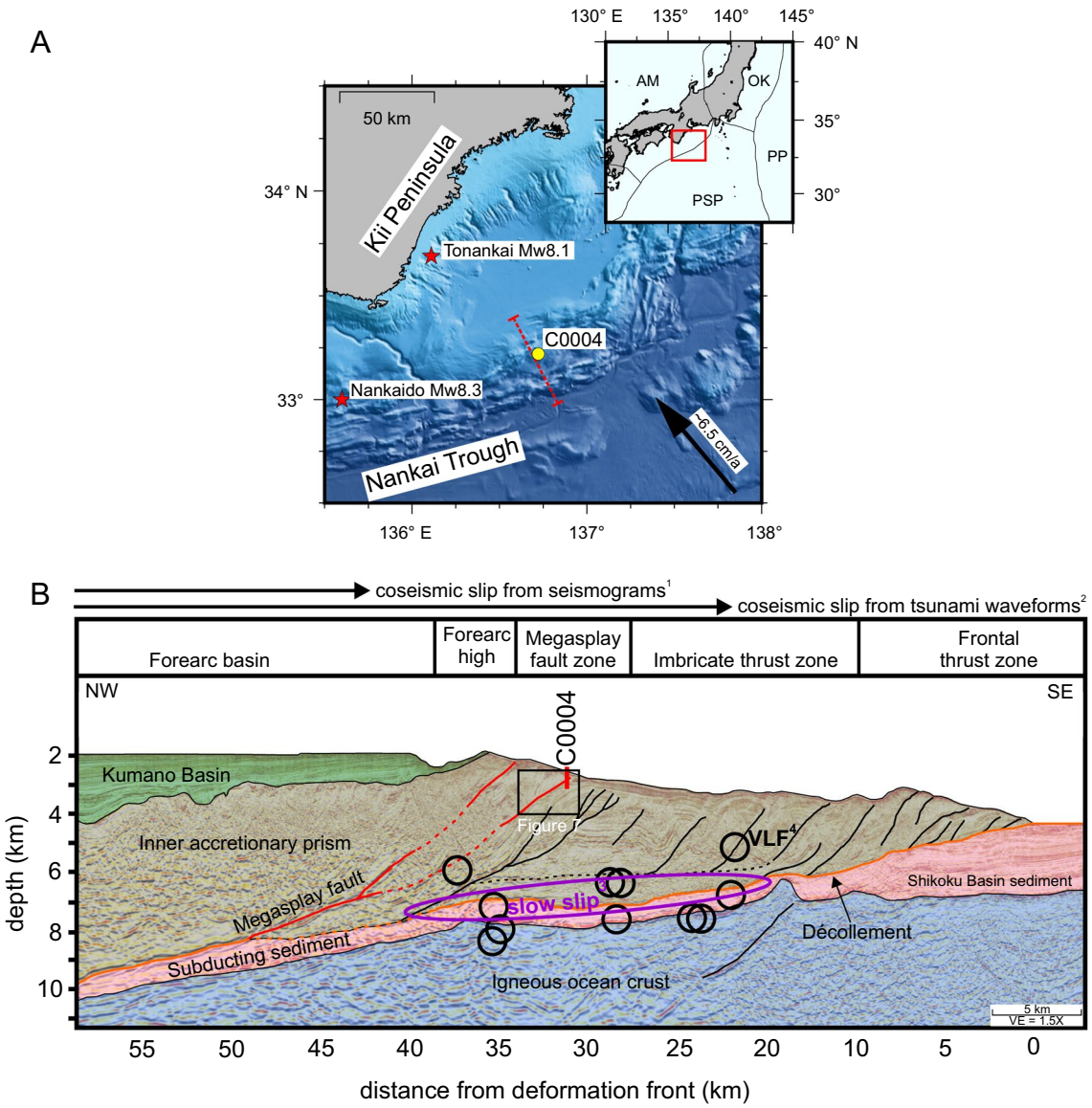

Fig. 1 Nankai Trough bathymetry and seismic cross section. **A** Bathymetric map (Olson et al. 2016) of the Nankai Trough area indicating drilling Site C0004 and the seismic cross section (red dashed line) shown in **B**. Megathrust earthquakes from the last century are shown as red stars. PSP: Philippine Sea Plate; PP: Pacific Plate; OK: Okhotsk Plate; Am: Amurian Plate. **B** The seismic cross section after Moore et al. (2009), showing the extent of coseismic slip of the Tonankai megathrust earthquake ([1]Kikuchi et al. (2003) and [2]Tanioka and Satake (2001)) as well as slow slip areas ([3]Araki et al. (2017)) and very low frequency earthquakes (VLF) ([4]Sugioka et al. (2012))

Within this framework, a decrease in steady-state frictional strength in response to increasing fault slip rate is known as velocity-weakening frictional behavior, whereas the opposite is termed velocity-strengthening frictional behavior. Velocity-strengthening behavior on faults tends to inhibit earthquake nucleation and favors steady creep. In contrast, velocity-weakening behavior, combined with specific elastic properties of the surrounding wall rock, is a prerequisite for earthquake nucleation and determines the type of earthquake (slip) expected along the fault zone. Some studies have also used RSF to describe landslide motion, where sliding on a basal plane is treated similarly to slip on a fault (Handwerger et al. 2016; Helmstetter et al. 2004; Lacroix et al. 2014).

RSF theory assumes steady-state sliding conditions, but experimental studies often show a slip dependence superimposed on the friction record during velocity step tests (Blanpied et al. 1998; Ikari et al. 2013; Ito and Ikari

2015; Roesner et al. 2020). These long-term slip weakening/strengthening trends are typically removed from the data to isolate the effect of the velocity change, and thus are not considered in frictional stability analyses (Blanpied et al. 1998). However, Ikari et al. (2013) analyzed the slip dependence in natural fault zone samples and showed that slip-weakening friction could allow sufficient slip instability for the occurrence of slow earthquakes in otherwise velocity-strengthening material. Furthermore, velocity perturbations, e.g., by foreshock afterslip, could induce slip weakening which may assist megathrust earthquake instability on natural faults by contributing to the stress drop (Ito et al. 2017; Ito and Ikari 2015). Ito and Ikari (2015) showed that the magnitude of slip-dependent frictional weakening could be large compared to velocity-dependent friction changes. Consequently, both slip and velocity dependence could affect the stability of a fault zone and should be considered to assess the potential for coseismic slip up to the seafloor and therefore the risk for tsunamigenesis.

Here, we use velocity stepping and constant velocity experiments simulating conditions from ~2–3 km depth up to the near seafloor to investigate the slip- and velocity dependence of friction of a natural sample from the megasplay fault zone in the Nankai Trough accretionary prism (Fig. 1). The observed frictional behavior is then discussed in terms of different modes of fault slip and potential geohazards originating on the megasplay fault.

Geological setting and sample description

The present-day Nankai Trough subduction zone is characterized by the subduction of the Philippine Sea plate under the Amurian microplate at a convergence rate of ~6.5 cm/year (Miyazaki and Heki 2001; Yokota et al. 2016). Offscraping of the incoming sediment cover has led to the formation of a >100-km-wide accretionary prism. The prism can be separated into an inner, stronger accretionary wedge and a weaker outer wedge, which is offset by a major out-of-sequence thrust fault named the "megasplay fault" (Kimura et al. 2007; Park et al. 2002; Strasser et al. 2009). The megasplay fault branches upward from the plate boundary thrust ~55 km landward of the deformation front up to the seafloor seaward of the outer ridge (Fig. 1B).

The shallow branches of the megasplay fault were drilled during Integrated Ocean Drilling Program (IODP) Expeditions 316, 319 and 365 at Sites C0004 and C0010 (Kinoshita et al. 2009; Saffer et al. 2010, 2017). We focus on Site C0004 (Fig. 1), where a wide fracture zone hosting the megasplay fault was sampled. IODP Site C0004 is well characterized by numerous friction studies testing fault zone and wall rock sediment (e.g., Ikari and Kopf 2017; Ikari and Saffer 2011; Roesner et al. 2020; Tsutsumi et al. 2011; Ujiie and Tsutsumi 2010). The hanging wall is composed of overriding accretionary prism sediment, whereas the footwall comprises underthrust slope sediment (Kimura et al. 2011). The fault zone at IODP Site C0004 spans from 256 to 315 m below seafloor (mbsf) and the deformed interval is composed of ash-bearing hemipelagic mud with some volcanic ash layers. The fault zone material on average is composed of 20% quartz, 18% feldspars, 2% calcite and 60% clay minerals (Kinoshita et al. 2009).

Experimental methods and procedure

We tested a sample from within the fault zone recovered from 277 mbsf (sample C0004D-29R-3), which has a mineralogical composition of 16% quartz, 18% feldspars, 48% phyllosilicates, 5% carbonates, 5% amphiboles and 8% other minerals with an abundance of 5% or less (Table 1). The mineralogical composition was determined by X-ray diffraction (XRD) analysis following Vogt et al. (2002). For these analyses, dried bulk samples were ground to a fine powder (<20 μm particle size) and loaded into a Philips X'Pert Pro multipurpose diffractometer. A double identification method was employed, where the first mineral identification was done using Philips software X'Pert HighScore™ and with the X-ray diffraction interpretation software MacDiff 4.25. Specific minerals, including individual clay species, were then determined based on the QUAX database, which contains several hundreds of reference minerals. Due to a limited amount of fault core material, we re-used the sediment for some experiments in this study. Comparing XRD analyses of the sample before and after an experiment showed that the effect of sample re-use is minor, with a post-experiment mineralogical composition of 18% quartz, 19% feldspars, and 42% phyllosilicates, 8% amorphous silica and 12% other minerals with an abundance of 5% or less (Table 1).

For the friction experiments, the sample material was dried in an oven at ~60 °C for >24 h, powdered with a mortar and pestle and sieved to a grain size of <180 μm. The powder was mixed with deionized water in a 2:1 ratio to form a stiff paste and placed in a stainless steel shearing assembly, which hosts the sample within a cylindrical volume having a diameter of 25.4 mm and a maximum height of 25 mm. The deionized water dissolves the salt crystals remaining in the oven-dried material to reconstitute seawater as pore fluid. Experiments were conducted in a direct shear configuration (GIESA RS5) (e.g., Ikari and Kopf 2011) at a constant room temperature of ~21 °C. For all experiments, the sample holder was flooded with artificial seawater with a salinity of 3.5%. (Additional file 2: Fig S1, Additional file 3: Fig. S2). The bottom and upper ends of the sample are connected via porous metal frits to an open water reservoir that ensures

Table 1 Sediment composition in weight percent (for abundances > 3 wt%) from X-ray diffraction measurements after Vogt et al. (2002)

Sample	Depth [mbsf]	Comment	Quartz	Plagioclase	K-feldspar	Sum carbonates	Amphiboles cordierite	SiO_2 nearly amorphous (Opal, glass)	Sum montmorillonites and smectites	Mixed layer clays	Illite	Glauconite	Kaolinite	Chlorite	Sum phyllosilicates
Error (rel.%)			±1	±2–5	±2–5	±2–3	±2–5	±5–10	±5	±5–10	±5–10	±5–10	±2–5	±2–5	±5
C0004D-29R-3	276.8–276.9	Before shearing	16	15	3	5	5	1	5	7	26	4	3	4	48
C0004D-29R-3	276.8–276.9	4× times remolding	18	16	3	3	1	8	3	12	20	0	3	4	42

Results of X-ray diffraction analysis and quantification of mineral phases based on the full-pattern method QUAX Vers.2018 (© 2018 Christoph Vogt, Central Laboratory for Crystallography and Applied Material Science, ZEKAM, Geosciences, University of Bremen)

pore water drainage. The samples were consolidated for 25 ± 2 h via a vertical piston which applied the normal stress σ_n, after which the sample height is typically ~ 15–20 mm. Changes in sample height became negligible after ~ 24 h of consolidation; thus we assume complete dissipation of pore water pressure. Consequently, the applied normal stress equals the effective normal stress σ_n'.

To shear the samples, the upper and the lower part of the shearing assembly are displaced relative to each other, which enforces localized shear perpendicular to the cylindrical axis of the sample. In our apparatus, the shear deformation behavior is measured in the top half of the sample, which is constantly aligned with the vertical piston applying the normal load. As the bottom half is sheared away, the top sample half comes into contact with the bottom plate of the steel sample holder, therefore the full area of the top half of the sample is always completely loaded and no area correction for the normal stresses is needed. Due to the geometry, there is progressively more sample-on-metal contact with increasing shear displacement, but we do not believe that this affects our results for two reasons: (1) Since our geologic samples are weaker than steel, deformation occurs in the sample rather than the metal sample holder, meaning we are recording the deformation properties of the sample and not the metal, and (2) Since the increase in sample-on-metal contact is geometric, it is constant with displacement for all samples. Thus, even if sliding against the sample cell had an effect on friction, the friction slip dependence can be compared for all samples at constant shear displacement. It also means that any variation in slip dependence must then be due to differences in the samples themselves. It can be seen in our previous work with the same apparatus (see for example the friction curves in Ikari 2019), that steady state is common, and that both slip weakening as well as slip strengthening are observed, indicating that sliding on the sample holder does not bias the friction slip dependence. Furthermore, we limit the total displacement in our experiments to 10 mm, such that sample-to-sample contact between the upper and lower sample halves is always greater than 50% of the total sliding surface area.

We tested σ_n' of 2, 4, 6, 10, 14 and 18 MPa; for every tested effective normal stress, we performed one velocity step experiment and two constant velocity experiments (without a velocity step). In the velocity step experiments, the samples were sheared at an initial shearing velocity $V_0 = 0.1$ µm/s for the first ~ 5 mm (run-in), followed by a velocity step increase to $V = 1.0$ µm/s for another 5 mm. During the constant velocity experiments, the shearing velocity (either 0.1 or 1.0 µm/s) was held constant for the entire 10 mm of displacement.

We report our results in terms of the coefficient of sliding friction μ, which is defined as the ratio of the measured shear stress (τ) to effective normal stress (σ_n'). Cohesion is often neglected in experimental friction studies, but recent studies showed that cohesive strength can be significant on mature clay-rich shear surfaces (Ikari and Kopf 2011; Roesner et al. 2020). Clay minerals dominate our sample material, thus our reported measurements include both cohesive and frictional strength.

The friction data from a velocity step test can be quantified as (Dieterich 1979, 1981; Marone 1998):

$$\mu = \mu_o + a\ln\left(\frac{V}{V_0}\right) + b_1 ln\left(\frac{V_0\theta_1}{D_{c1}}\right) + b_2 ln\left(\frac{V_0\theta_2}{D_{c2}}\right), \quad (1)$$

$$\frac{d\theta_i}{dt} = 1 - \frac{V\theta_i}{D_{ci}}, i = 1, 2, \quad (2)$$

where a, b_1, and b_2 are dimensionless parameters, θ_1 and θ_2 are state variables having units of time, and D_{c1} and D_{c2} are critical slip distances over which friction evolves to a new steady state. μ_o is the reference friction coefficient associated with the reference shearing velocity V_0 before the velocity step. If the experimental data are well described by one state variable, we set $b_2 = 0$. However, in some cases the data are clearly better described by two state variables, where we define $b = b_1 + b_2$. To evaluate our velocity step data and extract the RSF parameters, we modeled our velocity steps with an inverse modeling technique using a least-squares method established by Reinen and Weeks (1993) and in detail described by Skarbek and Savage (2019).

Under steady-state sliding conditions, the RSF law shown in Eqs. 1 and 2 reduces to:

$$a - b = \frac{\Delta\mu_{ss}}{ln\left(\frac{V}{V_0}\right)}, \quad (3)$$

where μ_{ss} is the friction coefficient at steady-state sliding and the parameter a-b quantifies the friction velocity dependence. Positive a-b values describe velocity-strengthening behavior that favors stable fault creep, where coseismic slip is resisted due to energy consumption by strengthening. In contrast, negative a-b values describe velocity-weakening behavior, which is a prerequisite for earthquake nucleation and a favorable condition for coseismic slip.

The RSF equations assume steady-state sliding conditions (i.e., that friction is independent of displacement) at both the initial and final sliding velocities. In most experiments, we observe a trend of slip dependence superimposed on the data which are commonly removed before the inversion (Blanpied et al. 1998; Ikari et al. 2013). Currently, there is no standardized method for removing a superimposed trend from the data. Often a linear curve

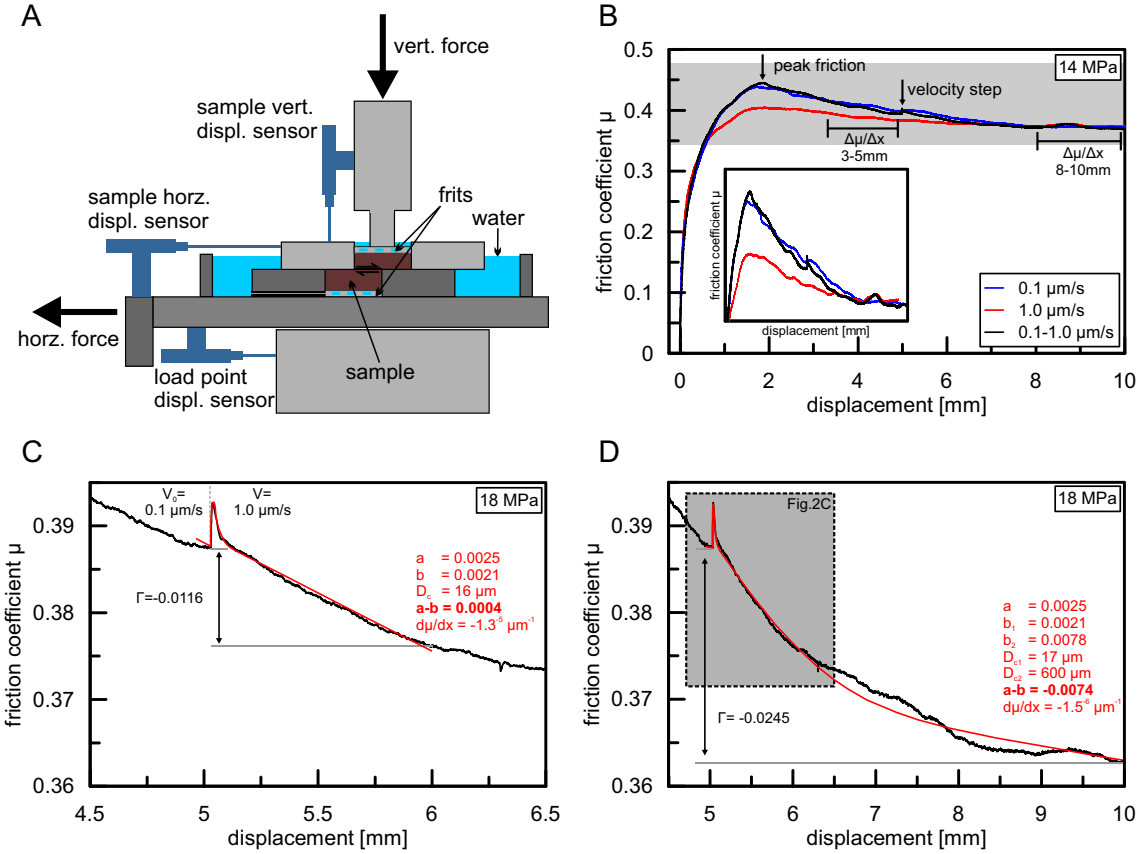

Fig. 2 Shear device and experimental data example. **A** Schematic diagram of the shear device used in this study. The lower sample cell holder (in darker grey) moves to the left as shearing is induced in the sample. **B** Example data from one set of experiments at conducted at 14 MPa effective normal stress, gray background indicates data shown in the inset. **C** Friction data during a velocity step overlain by modeled an inverse model over 1 mm, net change in frictional strength is shown as Γ. **D** Friction data during a velocity step modeled over 5 mm, net change in frictional strength again shown as Γ. VS: velocity step

fit is applied to the velocity step data to remove a superimposed trend, which can be an imprecise practice, especially if the trend is not linear or if different total slip distances are evaluated. This correction has a direct effect on $\Delta\mu_{ss}$, and therefore *a-b*. Commonly, data for individual velocity steps are evaluated over distances of < 1 mm after the step, to perform multiple velocity steps during an experiment. Here, we compare results of RSF modeling applied over the commonly used distance of approximately 1 mm, and also over an extended distance of 5 mm (e.g., Ito and Ikari 2015) (Fig. 2C, D).

To investigate the slip dependence of friction we measured the long-term trends in the friction data following the procedure of Ito and Ikari (2015). We quantified the slip dependence of friction with the parameter η, obtained by a linear fit to the friction data as:

$$\eta = \frac{\Delta\mu}{\Delta x}, \tag{4}$$

where x is the horizontal (shear) displacement. We measure η between 3 to 5 mm and 8 to 10 mm total slip displacement, with the velocity step occurring at 5 mm displacement (Fig. 2B). The first fitting window immediately precedes the velocity step, whereas the second fitting window evaluates the friction data at sufficient distance after the velocity step (~ 3 mm) in order to not be biased by the evolution effect following the velocity step. The same fitting procedure was done for the constant velocity experiments for comparison. We also determined the net change in frictional strength over 1 and 5 mm displacement following the velocity step, denoted as Γ:

$$\Gamma = \frac{\Delta\mu_i}{ln\left(\frac{V}{V_0}\right)}, \tag{5}$$

where μ_i is the instantaneous coefficient of friction. Equation 5 is not derived from the rate-and-state friction

formulation (Eqs. 1,2), and is intended to be used as a comparative measurement for shearing that is not necessarily at steady state (Ikari et al. 2020). The net change measurement Γ includes the effects of both the velocity- and slip-dependence of friction (Fig. 2C, D).

Results

The experimental shear stress curves as a function of displacement are typical of a highly consolidated clay, where linear elastic behavior is typically observed up to $\mu = \sim 0.2$ and displacements of a few tenths of a mm. This is followed by yielding and anelastic behavior up to the peak in friction, which is reached between 1 and 3 mm horizontal displacement. After the peak, frictional strength decreases over millimeter-scale slip distances (Fig. 2B). The peak friction coefficient in our experiments varies from 0.4 to 0.5 over the range of tested effective normal stresses and velocities (Fig. 3A). Peak friction for a shearing velocity of 0.1 µm/s decreases from 0.50 to 0.44 with increasing effective normal stress from 2 to 6 MPa, and remains nearly constant from 6 to 18 MPa. The peak friction measured at a shearing velocity of 1.0 µm/s is systematically smaller than the measurements at 0.1 µm/s, showing a decrease in peak friction from 0.46 to 0.40 between 2 – 6 MPa and also remaining nearly constant from 6 to 18 MPa. Although dilatancy is expected near the peak in friction (e.g., Mitchell and Soga 2005), this cannot be resolved from our measurements of vertical displacement due to an overall compaction trend during the experiment, likely caused by a small amount of sample extrusion (Scott et al. 1994).

The velocity-step experiments show mainly weakening, either expressed as velocity weakening or net weakening (Fig. 3B). Inverse modeling results of velocity step data over 1 mm show a-b values of -0.005 to 0.002, with velocity weakening at low effective normal stresses transitioning to velocity strengthening at an effective normal stress of 10 MPa. When the inverse model is applied over 5 mm displacement following the velocity step, larger velocity weakening (a-$b = -0.013$ to -0.002) independent of effective normal stress is observed. In comparison, net changes in friction coefficient exhibit larger absolute values of weakening. Net weakening measured 1 mm following the velocity steps ranges from $\Gamma = -0.025$ to -0.010, which decreases slightly as a function of effective normal stress. The largest net weakening is measured at 5 mm displacement beyond the velocity step ($\Gamma = -0.085$ to -0.025), which represents the largest values of

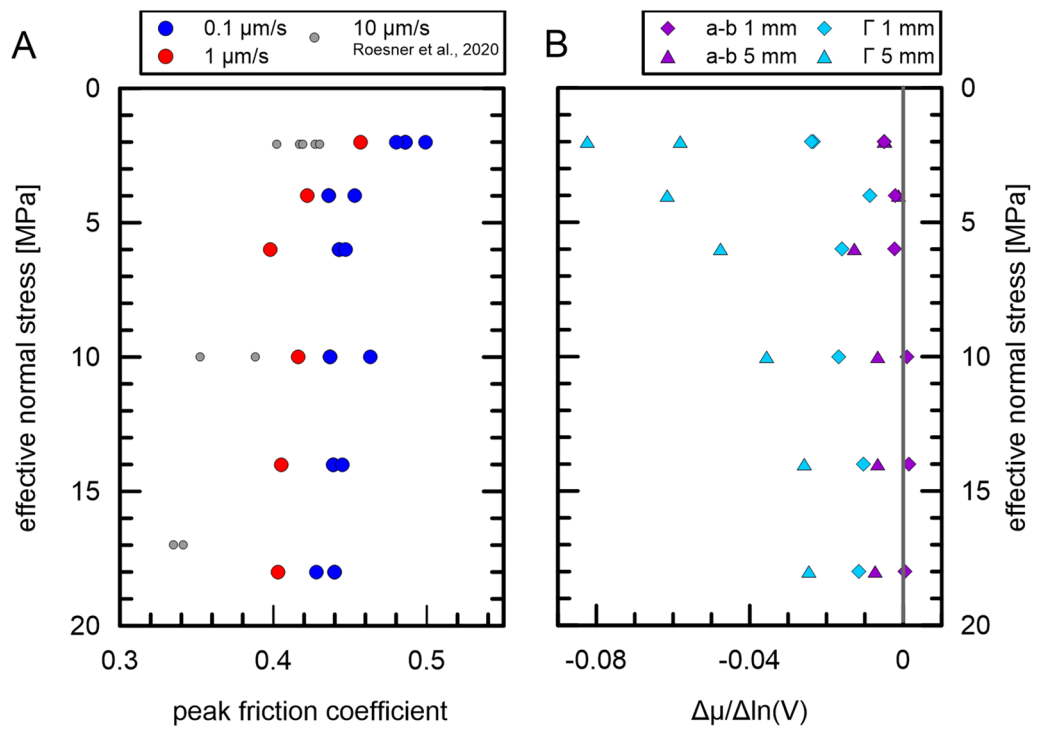

Fig. 3 Experimental results for peak friction and friction velocity dependence. **A** Peak friction as a function of effective normal stress. Grey circles represent C0004 megasplay fault peak friction data from Roesner et al. (2020). **B** Results of velocity stepping experiments showing modeled velocity dependence a-b as well as the net friction change Γ (see Eqs. 3 and 5)

weakening of any kind in this study (Fig. 3B). Net weakening at 5 mm correlates inversely with effective normal stress.

All experiments show slip weakening $\eta < 0$ over the tested range of horizontal displacements and effective normal stresses (Fig. 4A, B). With increasing effective normal stress, slip dependence becomes less negative, ranging from $\eta = -0.016$ to -0.024 mm^{-1} at 2 MPa, and $\eta = -0.004$ to -0.016 mm^{-1} at 18 MPa for 3–5 mm horizontal displacement (Fig. 4A). Slip weakening is more pronounced at lower velocities and lower displacements (Fig. 4A). Less slip weakening is observed at larger horizontal displacements of 8–10 mm, with $\eta = -0.014$ to -0.016 mm^{-1} at 2 MPa, and $\eta = -0.001$ to -0.003 mm^{-1} at 18 MPa. At high effective normal stresses, near-neutral η values are observed, indicating steady-state frictional behavior, whereas at low effective normal stresses steady-state friction is not established within 10 mm of shear displacement (Fig. 4B, C). Neither shearing velocity nor velocity perturbations (velocity step tests) systematically affect the weakening behavior at large displacements of the fault zone material (Fig. 4B).

Discussion

Mechanisms of observed behavior and comparison with previous results

When plotted as a function of effective normal stress, the peak shear strengths show a positive linear dependence with slopes of 0.40 (for 1 µm/s) and 0.44 (for 0.1 µm/s), exhibiting typical Mohr–Coulomb behavior (Additional file 4: Fig. S3). Our samples are normally consolidated because we use initially disaggregated sample powder, so we expect that the peak strengths are largely controlled by porosity. Following the peak, we observe large amounts of slip-weakening friction at low effective stresses, which approaches slip-neutral behavior (i.e., steady state) at higher effective normal stresses for the same displacement range. We interpret this to be caused by the faster development of a steady-state microstructure at higher stresses, which may include faster grain alignment, faster development of a pervasive foliation fabric, and the more rapid formation of a through-going shear band. These effects have been previously documented in sheared clay-rich materials at a wide range of effective normal stresses (Haines et al. 2009, 2013). Because our experiments show explicitly frictional weakening behavior that may be associated with developing microstructure, our results are most applicable to either newly developing faults, or mature faults that experience cyclic velocity changes and inter-event healing, which could alter or reset the

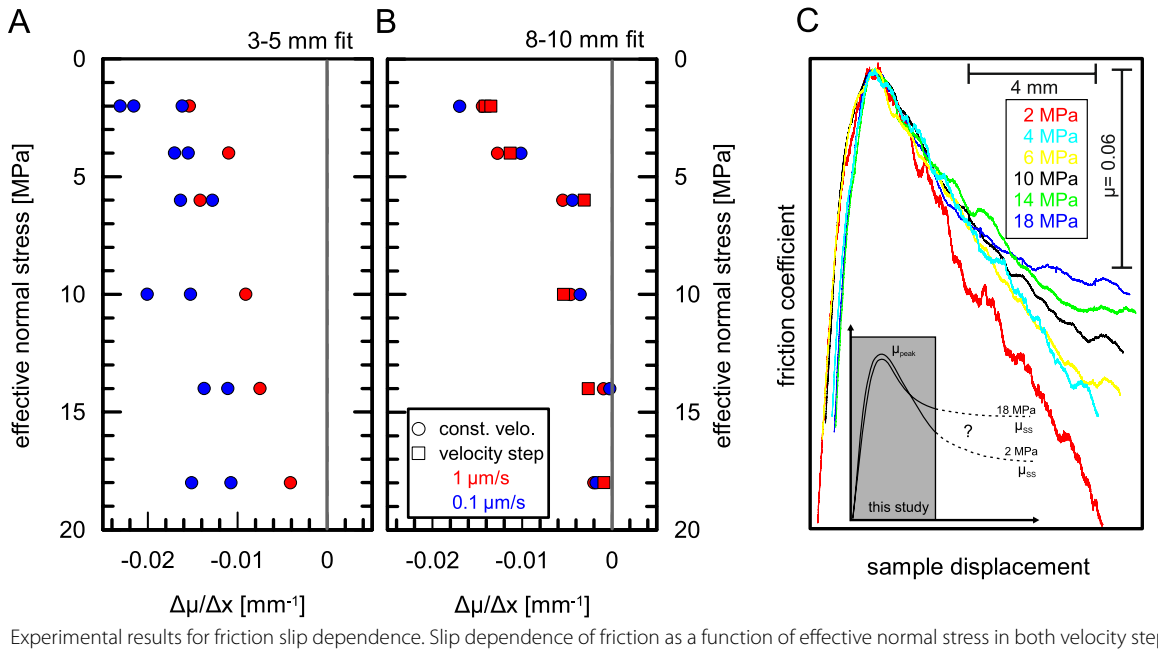

Fig. 4 Experimental results for friction slip dependence. Slip dependence of friction as a function of effective normal stress in both velocity step and constant velocity experiments. Friction slip dependence is shown for **A** 3–5 mm and **B** 8–10 mm displacement. **C** Friction-displacement curves for 0.1 µm/s graphically normalized by peak friction to illustrate slip weakening behavior from peak friction toward "steady-state". (Inset) Conceptual model of slip weakening behavior under varying effective normal stress. Gray represents data from our direct shear tests with 10 mm maximum displacement

sliding microstructure. Our results may not be relevant for mature faults that slide continuously at a constant velocity, although these may not be common in nature.

Measurements of friction slip dependence are not common, but we may compare our measurements of friction velocity dependence for "standard" slip distances of 1 mm with other friction studies of Nankai Trough materials. Although velocity-weakening friction is generally not expected in clay-rich materials (e.g., Ikari et al. 2009; Tembe et al. 2010), other previous studies have shown that when velocity weakening occurs in phyllosilicate gouges, it tends to be restricted to low normal stresses and low sliding velocities (e.g., Saffer et al. 2001; Ikari and Kopf 2017). This is consistent with the velocity-weakening friction we observe, which is limited to effective normal stresses of ≤ 6 MPa; at higher effective normal stresses we observe velocity-strengthening friction.

Despite the clay-rich nature of the Nankai Trough sediments, velocity-weakening friction has been observed in other friction studies testing materials from this subduction zone, and specifically from the modern outer accretionary prism (Tsutsumi et al. 2011; Roesner et al. 2020; Okuda et al. 2021). Although an earlier study found only velocity-strengthening friction for the megasplay (Ikari and Saffer 2011), this was later attributed to testing at higher than in situ stresses (Roesner et al. 2020). Other recent studies testing deeper (km-scale) material from the older, inner accretionary prism have shown consistent velocity-strengthening friction (Bedford et al. 2021; Fujioka et al. 2022), highlighting potentially fundamentally different behavior between the outer and inner prisms that may explain large-scale deformation behavior of the Nankai margin (Kimura et al. 2007). Roesner et al. (2020) noted that velocity-weakening in the megasplay samples showed larger values of the rate-and-state parameter b, and based on a microphysical explanation for rate-and-state frictional behavior (e.g., Dieterich and Kilgore 1994) suggested that the velocity weakening is somehow related to differences in the real area of contact as a function of effective normal stress.

Implications for shallow fault slip

Various fault slip styles such as slow slip events, very low frequency earthquakes and coseismic slip have been documented for the megasplay fault cutting through the Nankai accretionary prism (Araki et al. 2017; Ito and Obara 2006; Sugioka et al. 2012). For example, the tsunamigenic Nankaido and Tonankai earthquakes in 1944 and 1946 nucleated at seismogenic depth, and coseismic slip propagated upward along the pre-existing megasplay fault (Kame et al. 2003; Sakaguchi et al. 2011). Araki et al. (2017) documented similarly upward-migrating slow slip events which may have traveled along the megasplay fault. All of these fault slip events require a weakening mechanism, which would make it energetically favorable for slip to propagate updip along the fault. Figure 3B shows measurements of velocity weakening, and net weakening which includes the combined effects velocity and slip weakening, for the megasplay fault zone material. Velocity-weakening friction is necessary for earthquake nucleation and propagation (Dieterich 1986; Scholz 1998). Slip-weakening friction was suggested to be a potential mechanism for slip instability or quasi-instability resulting in slow slip (Ikari et al. 2013), although not necessarily for ordinary earthquakes. When only considering the data presented in Fig. 3B, it appears that slip weakening should be the dominant factor, especially at effective normal stresses < 10 MPa.

Although weakening is the prerequisite for all types of fault slip events, instability arises because of a disequilibrium between the wall rock and fault zone unloading stiffnesses. Fault instability in earthquake studies is often described by analogy to a spring-slider model, where instability occurs when the critical stiffness K_c defined by the fault zone properties is larger than the wall rock (or testing apparatus) stiffness K (Gu et al. 1984; Ruina 1983):

$$K < K_c = \frac{(b-a)\sigma_n^{'}}{D_c}. \tag{6}$$

The spring-slider model analogue is often used in earthquake nucleation studies, but can also be used for slow slip instability (Ikari 2019; Liu and Rice 2007; Shibazaki and Iio 2003). It can be seen that the critical stiffness is a function of the modeled friction parameters a and b (Scholz 2018) along with the effective normal stress (Fig. 5). In the case of two state variable modeling, we use the value of D_{c1} as D_c (Eq. 6) for critical stiffness evaluation. Equation 6 shows that instability can only arise on velocity-weakening faults because a shear stress drop is necessary. However, if slip weakening is considered it may also provide a stress drop. Ikari et al. (2013) proposed an additional instability criterion K_c^* based on a stress drop induced by the friction slip dependence η (Fig. 5):

$$K < K_c^* = -\eta\sigma_n^{'}. \tag{7}$$

We use the detrending parameter from our RSF modeling to calculate the short-distance slip-weakening rate $K_c^*{}_{1\ mm}$. $K_c^*{}_{5\ mm}$ for 5 mm displacement after the velocity step was calculated based on η measured for 8–10 mm displacement.

In the following, we compare the effects of friction velocity- and slip-dependence on slip stability using the

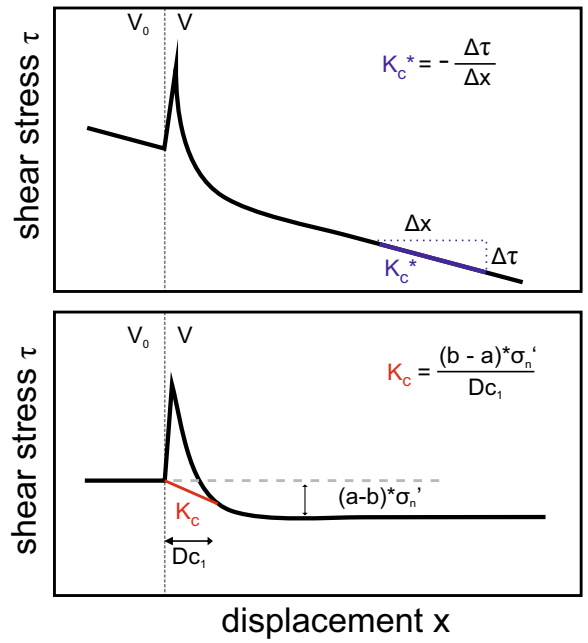

Fig. 5 Concept of critical stiffness. Schematic diagram showing a velocity step at low effective normal stress. **A** Determination of the critical stiffness for slip instability based friction slip dependence (Ikari et al. 2013). **B** Determination of the critical stiffness criterion based on RSF parameters derived from inverse modeling, including a linear detrending algorithm (Blanpied et al. 1998; Ruina 1983)

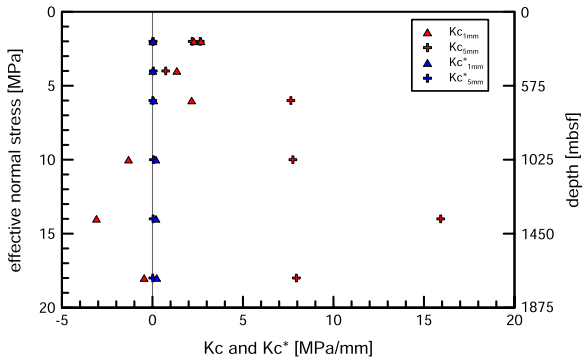

Fig. 6 Critical stiffness results. Velocity- and slip-dependent critical stiffnesses *Kc* and *Kc** as a function of effective normal stress. Depth calculation is based on shipboard moisture and density measurements, assuming hydrostatic pore water pressure

calculated K_c and K_c* values over both 1 and 5 mm of shear displacement. At high effective normal stresses, K_{c1mm} is negative and transitions to positive values between 6 and 10 MPa effective normal stress (Fig. 6), which is due to the change from velocity-weakening to velocity-strengthening behavior. Because the surrounding stiffness K is always positive, a negative critical stiffness value indicates that instability is impossible. At the lowest effective normal stress, K_{c1mm} exhibits its largest value of 3 MPa/mm. In contrast, K_{c5mm} shows mostly large positive critical stiffness values ranging from 1 to 16 MPa/mm. Over the tested range of effective normal stresses, K_c* is always positive with K_c*$_{1\ mm}$ ranging from 0.01 to 0.25 and K_c*$_{5\ mm}$ from 0.01 to 0.05 MPa/mm. Over the shorter slip distance, K_c* increases with increasing effective normal stress, whereas K_c* at larger slip distances does not show any systematic trend. Critical stiffnesses derived from velocity perturbations are ~ 2 orders of magnitude larger than those derived from slip dependence (Fig. 6 and Additional file 1: Table S1).

Our experiments show that weakening processes affecting slip propagation depend on both effective normal stress and slip distance. At effective normal stresses equivalent to depths < ~ 700 m, instability is facilitated by velocity-weakening friction at both small and large slip distances. Because the amount of weakening per slip from the velocity-weakening mechanism is about two orders of magnitude larger than that from the slip-weakening mechanism, slip dependence plays a minimal role for this particular depth condition (Fig. 7). At depths > 1000 m frictional behavior is more complex, due to pronounced slip distance effects for critical stiffnesses derived from the velocity dependence. Velocity-strengthening behavior for small displacements is expected to inhibit instability, but studies by Sakaguchi et al. (2011) and Araki et al. (2017) document evidence for fast and slow fault slip on the shallow branches of the megasplay fault in the Nankai subduction zone. A possible explanation for these observations might be instabilities caused by slip weakening, which overcomes the velocity strengthening at low slip distances. However, the critical stiffness values are very small and thus may allow slow fault slip to occur but not fast earthquakes. If slip weakening allows a large enough slip distance to be achieved, then greater instability can occur due to the large-distance velocity weakening, which increases the critical stiffness value. Therefore, for depths > ~ 1000 m we suggest a hybrid mechanism, where instability is initially caused by slip weakening which is then further driven by velocity weakening over longer distances. Taken together, our data and critical stiffness analyses suggest that the sliding behavior of the megasplay fault becomes progressively more unstable with decreasing effective normal stress. Thus, we infer that the frictional behavior of the megasplay material will tend to assist slip events migrating updip towards the seafloor.

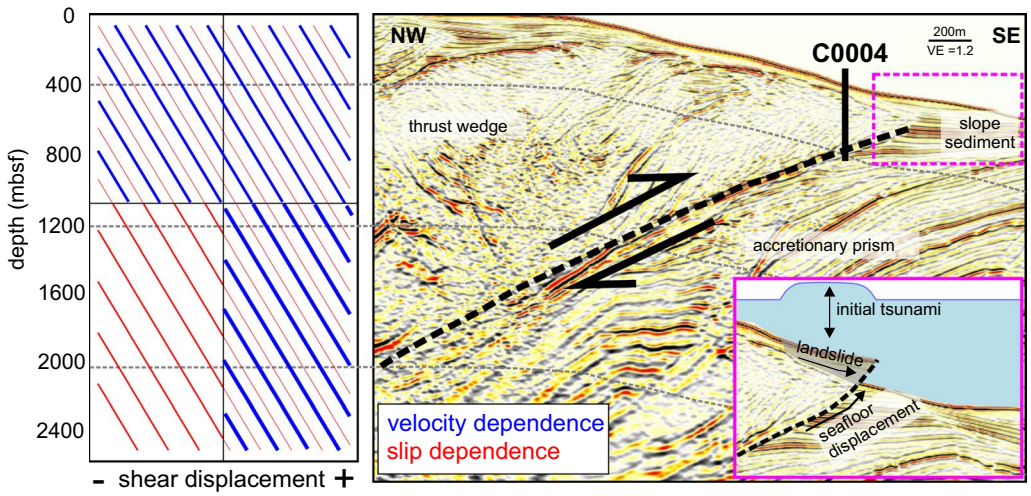

Fig. 7 Friction along the megasplay fault. Seismic cross section of Site C0004 showing how friction slip and velocity dependence is expected to evolve with depth along the megasplay fault. At deeper depths, slip dependence is the mechanism facilitating instability at short displacements, but at larger shear displacement the friction velocity dependence becomes dominant. At shallow depths, the friction velocity dependence is dominant for both short and large shear displacement. Line thicknesses illustrate the relative magnitude of the velocity and slip dependence. Depth is extrapolated from effective normal stress calculations from shipboard bulk density measurements on the cored interval. The overview map is shown in Fig. 1. Inset indicates natural hazards associated with megasplay slip deforming the seafloor

Implications for submarine landslides

Extrapolating our results to the seafloor suggests that large slip weakening and higher peak friction coefficient should be expected at effective normal stresses < 2 MPa, which translates to depths of ~ 0–200 mbsf, where submarine landslides occur (Fig. 7). The fundamental requirement for slope failure is that the shear stresses on the potential failure plane exceed the shear strength of the slope sediment (Morgenstern 1967). Our laboratory measurements are relevant for submarine landslides in two ways. First, they directly characterize the sediment strength, where the larger peak friction coefficient we observe under low effective normal stresses may slightly reduce the risk for slope failure initiation, but the measured slip weakening (in landslide studies often named brittle soil behavior) (Duncan et al. 2014) is associated with progressive slope failure phenomena (Troncone 2005). The progressive failure mechanism occurs primarily in strain-softening soil, where after an initial peak the shear strength reduces to a lower residual value. This reduction of shear strength will increase the shear stress on neighboring soil elements, causing progressive failure (Skempton 1964).

At the Nankai subduction zone, evidence for sediment mass transports in the shallow megasplay fault zone (Fig. 1B) have been identified in seismic and bathymetric data, and also in core samples (Kanamatsu et al. 2014; Strasser et al. 2011). These mass-wasting events occurred at times of enhanced megasplay fault activity (Strasser et al. 2011). Therefore, the second way in which the strength patterns we observe affect submarine landslides, is that they may allow slip to reach near-seafloor depths, causing local steepening of the seafloor slope. Whereas seafloor-breaching coseismic slip directly causes tsunamis, SSEs are slow compared to their fast counterparts and are unlikely to trigger tsunamigenesis by rapid seafloor displacement. However, SSEs propagating up to the seafloor will deform the seafloor topography and might cause an increase in the seafloor slope angle, which is a preconditioning factor for submarine landslides by increasing the stress on the sediment (Hampton et al. 1996) (Fig. 7 inset). When they occur, submarine landslides themselves may be a source of tsunamigenesis by displacing large amounts of ocean water (Baba et al. 2019; Harbitz et al. 2006; Ward 2001). Thus, shallow upward-propagating SSEs should be regarded as a long-term enhancement factor for submarine landslide and tsunami hazards in subduction zones.

Conclusions

The RSF framework is a powerful tool to quantify the friction velocity dependence of experimental data, but slip-dependent friction trends, which are typically removed from the data, also hold important information describing fault gouge behavior under shear. We combine measurements of slip and velocity-dependent friction in a comprehensive frictional stability analysis of the shallow Nankai Trough megasplay fault. The IODP

Site C0004 fault samples exhibit both velocity- and slip-dependent weakening, with velocity weakening having a larger effect on slip stability. We find that velocity-weakening friction is more pronounced at shallow depths, and can explain slip instability without the need to invoke slip weakening at both the short and long displacements considered in this study. At deeper depths, slip-weakening friction may be necessary to overcome short-distance velocity-strengthening friction before velocity-weakening at larger displacements might become dominant. Sediments characterized by slip instability in the shallow accretionary prism may facilitate seafloor deformation. Therefore, the weakening behavior of the megasplay fault sediment at shallow depths is favorable for tsunamigenesis, either directly by seafloor-breaching slip events or indirectly by submarine landslides.

Abbreviations

SSE: Slow slip event; VLFE: Very low frequency earthquake; RSF: Rate- and state-dependent friction; VS: Velocity step experiment; VE: Vertical exaggeration.

Supplementary Information

The online version contains supplementary material available at https://doi.org/10.1186/s40623-022-01728-w.

Additional file 1: Table S1. Experimental table. All velocity step and constant velocity experiments are shown with friction dependence parameters as well as modeling parameters for the velocity step tests.

Additional file 2: Figure S1. Technical drawing of the sample holder configuration, indicating possible drainage pathways in blue.

Additional file 3: Figure S2. Experimental data showing friction coefficient as a function of shear displacement for all experiments. Friction coefficient is either expressed in absolute values or normalized by peak friction. VS = velocity step experiment.

Additional file 4: Figure S3. Direct shear test results, showing (A) friction as a function of displacement at a constant velocity of 1.0 µm/s, and (B) constant velocity 0.1 µm/s. Peak friction values are plotted as a function of effective normal stress in the right-hand panels of (A) and (B), which show fitted peak friction values of 0.40 (A) and 0.44 (B) as the slopes to linear fits.

Acknowledgements

This study used samples drilled by the D/V Chikyu from the Integrated Ocean Drilling Program (IODP). We would like to thank the staff, the drilling personnel, and the technicians (Marine Works Japan) for their effort and support during the drilling expedition. XRD measurements were done by Dr. Christoph Vogt in the research group crystallography of the University of Bremen. We thank Gregory F. Moore (University of Hawaii) for providing the seismic image of the megasplay fault (Fig.7). We also thank Katja Stanislowski and Aagje Eijsink for insightful discussions of experimental results and Philipp Haberkorn for technical support. Frictional data were modelled with the program "Xlook" courtesy of Chris Marone. We thank John Bedford and an anonymous reviewer for helpful comments that improved this manuscript.

Author contributions

AR, MJI, AH, AJK designed the study. AR performed all experiments and analyzed the data. AR and MJI interpreted the data and drafted the manuscript. AH and AJK reviewed the manuscript and provided feedback. All authors read and approved the final manuscript.

Funding

Open Access funding enabled and organized by Projekt DEAL. This project has received funding from the European Research Council (ERC) under the European Union's Horizon 2020 research and innovation program (Grant Agreement No. 714430 to MJI) as well as from the Deutsche Forschungsgemeinschaft (DFG KO2108/24-1 to AJK).

Availability of data and materials

All data generated or analyzed during this study are included in this published article [and its supplementary information files].

Declarations

Ethics approval and consent to participate

Not applicable.

Consent for publication

Not applicable.

Competing interests

The authors declare that they have no competing interests.

Received: 30 June 2022 Accepted: 20 October 2022
Published online: 04 November 2022

References

Ando M (1975a) Possibility of a major earthquake in the Tokai district, Japan and its pre-estimated seismotectonic effects. Tectonophysics 25:69–85. https://doi.org/10.1016/0040-1951(75)90011-6

Ando M (1975b) Source mechanisms and tectonic significance of historical earthquakes along the Nankai trough, Japan. Tectonophysics 27:119–140. https://doi.org/10.1016/0040-1951(75)90102-X

Ando M (1982) A fault model of the 1946 Nankaido earthquake derived from tsunami data. Phys Earth Planet Inter 28:320–336. https://doi.org/10.1016/0031-9201(82)90089-9

Annoura S, Hashimoto T, Kamaya N, Katsumata A (2017) Shallow episodic tremor near the Nankai Trough axis off southeast Mie prefecture, Japan. Geophys Res Lett 44:3564–3571. https://doi.org/10.1002/2017GL073006

Araki E, Saffer DM, Kopf AJ, Wallace LM, Kimura T, Machida Y, Ide S, Davis E, IODP Expedition 365 shipboard scientist (2017) Recurring and triggered slow-slip events near the trench at the Nankai Trough subduction megathrust. Science 356:1157–1160. https://doi.org/10.1126/science.aan3120

Baba T, Gon Y, Imai K, Yamashita K, Matsuno T, Hayashi M, Ichihara H (2019) Modeling of a dispersive tsunami caused by a submarine landslide based on detailed bathymetry of the continental slope in the Nankai trough, southwest Japan. Tectonophysics 768:228182. https://doi.org/10.1016/j.tecto.2019.228182

Bedford JD, Faulkner DR, Allen MJ, Hirose T (2021) The stabilizing effect of high pore-fluid pressure along subduction megathrust faults: evidence from friction experiments on accretionary sediments from the Nankai Trough. Earth Planet Sci Lett 574:117161. https://doi.org/10.1016/j.epsl.2021.117161

Bilek SL, Lay T (2002) Tsunami earthquakes possibly widespread manifestations of frictional conditional stability. Geophys Res Lett 29:18. https://doi.org/10.1029/2002GL015215

Blanpied ML, Marone CJ, Lockner DA, Byerlee JD, King DP (1998) Quantitative measure of the variation in fault rheology due to fluid-rock interactions. J Geophys Res 103:9691–9712. https://doi.org/10.1029/98JB00162

Dieterich JH (1979) Modeling of rock friction: 1. Experimental results and constitutive equations. J Geophys Res 84:2161. https://doi.org/10.1029/JB084iB05p02161

Dieterich JH (1981) Constitutive Properties of Faults With Simulated Gouge. In: Mechanical Behavior of Crustal Rocks: The Handin Volume. American Geophysical Union, pp 103–120. https://doi.org/10.1029/GM024p0103

Dieterich JH (1986) A model for the nucleation of earthquake slip. Earthq Source Mech 37:37–47. https://doi.org/10.1029/GM037p0037

Dieterich JH, Kilgore BD (1994) Direct observation of frictional contacts: new insights for state-dependent properties. Pure Appl Geophys 143:283–302. https://doi.org/10.1007/BF00874332
Duncan JM, Wright SG, Brandon TL (2014) Soil strength and slope stability. Wiley, Hoboken, New Jersey
Faulkner DR, Mitchell TM, Behnsen J, Hirose T, Shimamoto T (2011) Stuck in the mud?: Earthquake nucleation and propagation through accretionary forearcs. Geophys Res Lett 38:1–5. https://doi.org/10.1029/2011GL048552
Fujioka R, Katayama I, Kitamura M, Okuda H, Hirose T (2022) Depth profile of frictional properties in the inner Nankai accretionary prism using cuttings from IODP Site C0002. Prog Earth Planet Sci 9:31. https://doi.org/10.1186/s40645-022-00488-1
Gu J-C, Rice JR, Ruina AL, Tse ST (1984) Slip motion and stability of a single degree of freedom elastic system with rate and state dependent friction. J Mech Phys Solids 32:167–196. https://doi.org/10.1016/0022-5096(84)90007-3
Haines SH, van der Pluijm BA, Ikari MJ, Saffer DM, Marone C (2009) Clay fabric intensity in natural and artificial gouges: Implications for brittle fault zone processes and sedimentary basin clay fabric evolution. J Geophys Res Solid Earth 114:B05406. https://doi.org/10.1029/2008JB005866
Haines SH, Kaproth B, Marone C, Saffer D, van der Pluijm B (2013) Shear zones in clay-rich fault gouge: a laboratory study of fabric development and evolution. J Struct Geol 51:206–225. https://doi.org/10.1016/j.jsg.2013.01.002
Hampton MA, Lee HJ, Locat J (1996) Submarine landslides. Rev Geophys 34:33–59. https://doi.org/10.1029/95RG03287
Handwerger AL, Rempel AW, Skarbek RM, Roering JJ, Hilley GE (2016) Rate-weakening friction characterizes both slow sliding and catastrophic failure of landslides. Proc Natl Acad Sci USA 113:10281–10286. https://doi.org/10.1073/pnas.1607009113
Harbitz CB, Løvholt F, Pedersen G, Masson DG (2006) Mechanisms of tsunami generation by submarine landslides: a short review. Norw J Geol 86:255–264
Helmstetter A, Sornette D, Grasso J-R, Andersen JV, Gluzman S, Pisarenko V (2004) Slider block friction model for landslides: application to Vaiont and La Clapière landslides. J Geophys Res. https://doi.org/10.1029/2002JB002160
Hirose T, Hiramatsu Y, Obara K (2010) Characteristics of short-term slow slip events estimated from deep low-frequency tremors in Shikoku, Japan. J Geophys Res 115:B00A05. https://doi.org/10.1029/2010JB007608
Ichinose GA, Thio HK, Somerville PG, Sato T, Ishii T (2003) Rupture process of the 1944 Tonankai earthquake (Ms 8.1) from the inversion of teleseismic and regional seismograms. J Geophys Res 108:119. https://doi.org/10.1029/2003JB002393
Ide S (2012) Variety and spatial heterogeneity of tectonic tremor worldwide. J Geophys Res 117:3. https://doi.org/10.1029/2011JB008840
Ikari MJ (2019) Laboratory slow slip events in natural geological materials. Geophys J Int 218:354–387. https://doi.org/10.1093/gji/ggz143
Ikari MJ, Kopf AJ (2011) Cohesive strength of clay-rich sediment. Geophys Res Lett. https://doi.org/10.1029/2011GL047918
Ikari MJ, Kopf AJ (2017) Seismic potential of weak, near-surface faults revealed at plate tectonic slip rates. Sci Adv 3:e1701269. https://doi.org/10.1126/sciadv.1701269
Ikari MJ, Saffer DM (2011) Comparison of frictional strength and velocity dependence between fault zones in the Nankai accretionary complex. Geochem Geophys Geosyst 12:1–16. https://doi.org/10.1029/2010GC003442
Ikari MJ, Saffer DM, Marone C (2009) Frictional and hydrologic properties of clay-rich fault gouge. J Geophys Res Solid Earth 114:B05409. https://doi.org/10.1029/2008JB006089
Ikari MJ, Marone C, Saffer DM, Kopf AJ (2013) Slip weakening as a mechanism for slow earthquakes. Nature Geosci 6:468–472. https://doi.org/10.1038/ngeo1818
Ikari MJ, Carpenter BM, Scuderi MM, Collettini C, Kopf AJ (2020) Frictional strengthening explored during non-steady state shearing: implications for fault stability and slip event recurrence time. J Geophys Res Solid Earth. https://doi.org/10.1029/2020JB020015
Ito Y, Ikari MJ (2015) Velocity- and slip-dependent weakening in simulated fault gouge: implications for multimode fault slip. Geophys Res Lett 42:9247–9254. https://doi.org/10.1002/2015GL065829
Ito Y, Obara K (2006) Very low frequency earthquakes within accretionary prisms are very low stress-drop earthquakes. Geophys Res Lett 33:1131. https://doi.org/10.1029/2006GL025883
Ito Y, Ikari MJ, Ujiie K, Kopf A (2017) Coseismic slip propagation on the Tohoku plate boundary fault facilitated by slip-dependent weakening during slow fault slip. Geophys Res Lett 44:8749–8756. https://doi.org/10.1002/2017GL074307
Kame N, Rice JR, Dmowska R (2003) Effects of prestress state and rupture velocity on dynamic fault branching. J Geophys Res 108:5679. https://doi.org/10.1029/2002JB002189
Kanamatsu T, Kawamura K, Strasser M, Novak B, Kitamura Y (2014) Flow dynamics of Nankai Trough submarine landslide inferred from internal deformation using magnetic fabric. Geochem Geophys Geosyst 15:4079–4092. https://doi.org/10.1002/2014GC005409
Kikuchi M, Nakamura M, Yoshikawa K (2003) Source rupture processes of the 1944 Tonankai earthquake and the 1945 Mikawa earthquake derived from low-gain seismograms. Earth Planet Space 55:159–172. https://doi.org/10.1186/BF03351745
Kimura G, Kitamura Y, Hashimoto Y, Yamaguchi A, Shibata T, Ujiie K, Okamoto S (2007) Transition of accretionary wedge structures around the up-dip limit of the seismogenic subduction zone. Earth Planet Sci Lett 255:471–484. https://doi.org/10.1016/j.epsl.2007.01.005
Kimura G, Moore GF, Strasser M, Screaton E, Curewitz D, Streiff C, Tobin H (2011) Spatial and temporal evolution of the megasplay fault in the Nankai Trough. Geochem Geophys Geosyst. https://doi.org/10.1029/2010GC003335
Kinoshita M, Tobin H, Ashi J, Kimura G, Lallemant S, Screaton EJ, Curewitz D, Masago H, Moe KT, Expedition 314/315/316 Scientists (2009) Proc. IODP, 314/315/316: Washington, DC (Integrated Ocean Drilling Program Management International, Inc.). https://doi.org/10.2204/iodp.proc.314315316.2009
Lacroix P, Perfettini H, Taipe E, Guillier B (2014) Coseismic and postseismic motion of a landslide: observations, modeling, and analogy with tectonic faults. Geophys Res Lett 41:6676–6680. https://doi.org/10.1002/2014GL061170
Liu Y, Rice JR (2007) Spontaneous and triggered aseismic deformation transients in a subduction fault model. J Geophys Res. https://doi.org/10.1029/2007JB004930
Marone C (1998) Laboratory-derived friction laws and their application to seismic faulting. Annu Rev Earth Planet Sci 26:643–696. https://doi.org/10.1146/annurev.earth.26.1.643
Marone C, Scholz CH (1988) The depth of seismic faulting and the upper transition from stable to unstable slip regimes. Geophys Res Lett 15:621–624. https://doi.org/10.1029/GL015i006p00621
Mitchell JK, Soga K (2005) Fundamentals of soil behavior, vol 3. Wiley, New York
Miyazaki S, Heki K (2001) Crustal velocity field of southwest Japan: subduction and arc-arc collision. J Geophys Res 106:4305–4326. https://doi.org/10.1029/2000JB900312
Moore GF, Park J-O, Bangs NL, Gulick SP, Tobin HJ, Nakamura Y, Saito S, Tsuji T, Yoro T, Tanaka H, Uraki S, Kido Y, Sanada Y, Kuramoto S, Taira A (2009) Structural and seismic stratigraphic framework of the NanTroSEIZE Stage 1 transect. In: Kinoshita M, Tobin H, Ashi J, Kimura G, Lallemant S, Screaton E, Curewitz D, Masago H, Moe K, the Expedition 314/315/316 Scientists (eds) NanTroSEIZE Stage 1: investigations of seismogenesis, Nankai Trough, Japan. Integrated Ocean Drilling Program, Washington
Morgenstern NR (1967) Submarine slumping and the initiation of turbidity currents. Marine Geotechnique 3:189–220
Nakano M, Hori T, Araki E, Kodaira S, Ide S (2018) Shallow very-low-frequency earthquakes accompany slow slip events in the Nankai subduction zone. Nat Commun 9:984. https://doi.org/10.1038/s41467-018-03431-5
Obara K, Ito Y (2005) Very low frequency earthquakes excited by the 2004 off the Kii peninsula earthquakes: a dynamic deformation process in the large accretionary prism. Earth Planet Space 57:321–326. https://doi.org/10.1186/BF03352570
Okuda H, Ikari MJ, Roesner A, Stanislowski K, Hüpers A, Yamaguchi A, Kopf AJ (2021) Spatial patterns in frictional behavior of sediments along the Kumano transect in the Nankai Trough. J Geophys Res Solid Earth 126:e2021JB022546. https://doi.org/10.1029/2021JB022546
Olson CJ, Becker JJ, Sandwell DT (2016) SRTM15_PLUS: Data fusion of Shuttle Radar Topography Mission (SRTM) land topography with measured and estimated seafloor topography (NCEI Accession 0150537)

Park J-O, Tsuru T, Kodaira S, Cummins PR, Kaneda Y (2002) Splay fault branching along the Nankai subduction zone. Science 297:1157–1160. https://doi.org/10.1126/science.1074111
Polet J, Kanamori H (2000) Shallow subduction zone earthquakes and their tsunamigenic potential. Geophys J Int 142:684–702. https://doi.org/10.1046/j.1365-246x.2000.00205.x
Reinen LA, Weeks JD (1993) Determination of rock friction constitutive parameters using an iterative least squares inversion method. J Geophys Res 98:15937. https://doi.org/10.1029/93JB00780
Roesner A, Ikari MJ, Saffer DM, Stanislowski K, Eijsink AM, Kopf AJ (2020) Friction experiments under in-situ stress reveal unexpected velocity-weakening in Nankai accretionary prism samples. Earth Planet Sci Lett 538:116180. https://doi.org/10.1016/j.epsl.2020.116180
Ruina A (1983) Slip instability and state variable friction laws. J Geophys Res 88:10359–10370. https://doi.org/10.1029/JB088iB12p10359
Saffer DM, Frye KM, Marone C, Mair K (2001) Laboratory results indicating complex and potentially unstable frictional behavior of smectite clay. Geophys Res Lett 28:2297–2300. https://doi.org/10.1029/2001GL012869
Saffer D, McNeill L, Byrne T, Araki E, Toczko S, Eguchi N, Takahashi K, Expedition 319 Scientists (2010) Proc. IODP, 319: Tokyo (Integrated Ocean Drilling Program Management International, Inc.). https://doi.org/10.2204/iodp.proc.319.2010
Saffer D, Kopf A, Toczko S, Expedition 365 Scientists (2017) Proc. IODP, 365: College Station, TX (International Ocean Discovery Program). https://doi.org/10.14379/iodp.proc.365.2017
Sakaguchi A, Chester F, Curewitz D, Fabbri O, Goldsby D, Kimura G, Li C-F, Masaki Y, Screaton EJ, Tsutsumi A, Ujiie K, Yamaguchi A (2011) Seismic slip propagation to the updip end of plate boundary subduction interface faults: Vitrinite reflectance geothermometry on Integrated Ocean Drilling Program NanTro SEIZE cores. Geology 39:395–398. https://doi.org/10.1130/G31642.1
Scholz CH (1998) Earthquakes and friction laws. Nature 391:37–42. https://doi.org/10.1038/34097
Scholz CH (2018) The mechanics of earthquakes and faulting. Cambridge University Press, Cambridge
Scott DR, Marone CJ, Sammis CG (1994) The apparent friction of granular fault gouge in sheared layers. J Geophys Res 99:7231–7246. https://doi.org/10.1029/93JB03361
Seno T (2002) Tsunami earthquakes as transient phenomena. Geophys Res Lett 29:58. https://doi.org/10.1029/2002GL014868
Shibazaki B, Iio Y (2003) On the physical mechanism of silent slip events along the deeper part of the seismogenic zone. Geophys Res Lett 30:1525. https://doi.org/10.1029/2003GL017047
Skarbek RM, Savage HM (2019) RSFit3000: A MATLAB GUI-based program for determining rate and state frictional parameters from experimental data. Geosphere 15:1665–1676. https://doi.org/10.1130/GES02122.1
Skempton AW (1964) Long-term stability of clay slopes. Géotechnique 14:77–102. https://doi.org/10.1680/geot.1964.14.2.77
Strasser M, Moore GF, Kimura G, Kitamura Y, Kopf AJ, Lallemant S, Park J-O, Screaton EJ, Su X, Underwood MB, Zhao X (2009) Origin and evolution of a splay fault in the Nankai accretionary wedge. Nat Geosci 2:648–652. https://doi.org/10.1038/ngeo609
Strasser M, Moore GF, Kimura G, Kopf AJ, Underwood MB, Guo J, Screaton EJ (2011) Slumping and mass transport deposition in the Nankai fore arc: evidence from IODP drilling and 3-D reflection seismic data. Geochem Geophys Geosyst. https://doi.org/10.1029/2010GC003431
Sugioka H, Okamoto T, Nakamura T, Ishihara Y, Ito A, Obana K, Kinoshita M, Nakahigashi K, Shinohara M, Fukao Y (2012) Tsunamigenic potential of the shallow subduction plate boundary inferred from slow seismic slip. Nature Geosci 5:414–418. https://doi.org/10.1038/ngeo1466
Tanioka Y, Satake K (2001) Detailed coseismic slip distribution of the 1944 Tonankai earthquake estimated from tsunami waveforms. Geophys Res Lett 28:1075–1078. https://doi.org/10.1029/2000GL012284
Tembe S, Lockner DA, Wong T-F (2010) Effect of clay content and mineralogy on frictional sliding behavior of simulated gouges: binary and ternary mixtures of quartz, illite and montmorillonite. J Geophys Res Solid Earth 115:B03416. https://doi.org/10.1029/2009JB006383
Troncone A (2005) Numerical analysis of a landslide in soils with strain-softening behaviour. Géotechnique 55:585–596. https://doi.org/10.1680/geot.2005.55.8.585
Tsutsumi A, Fabbri O, Karpoff AM, Ujiie K, Tsujimoto A (2011) Friction velocity dependence of clay-rich fault material along a megasplay fault in the Nankai subduction zone at intermediate to high velocities. Geophys Res Lett. https://doi.org/10.1029/2011GL049314
Ujiie K, Tsutsumi A (2010) High-velocity frictional properties of clay-rich fault gouge in a megasplay fault zone, Nankai Subduction Zone. Geophys Res Lett. https://doi.org/10.1029/2010GL046002
Vogt C, Fischer RX, Lauterjung J (2002) Investigation of the clay fraction (<2 µm) of the clay mineral society reference clays. Clays Clay Miner 50:388–400
Ward SN (2001) Landslide tsunami. J Geophys Res 106:11201–11215. https://doi.org/10.1029/2000JB900450
Yokota Y, Ishikawa T, Watanabe S, Tashiro T, Asada A (2016) Seafloor geodetic constraints on interplate coupling of the Nankai Trough megathrust zone. Nature 534:374–377. https://doi.org/10.1038/nature17632

Publisher's Note